



Cite this: *J. Mater. Chem. C*, 2023,
11, 8121

High-performance semitransparent organic solar cells based on sequentially processed heterojunction†

Peiyao Xue,^a Jingming Xin,^c Guanyu Lu,^d Boyu Jia,^a Heng Lu,^a Guanghao Lu,^d Wei Ma,^c Ray P. S. Han^e and Xiaowei Zhan^{†,ab}

Average visible transmittance (AVT) and power conversion efficiency (PCE) are the two key parameters to evaluate the performance of semitransparent organic solar cells (ST-OSCs). Reducing the donor content can decrease the light absorption in the visible region and increase the AVT values of ST-OSCs. However, minor donor phase is not sufficient for exciton generation, exciton dissociation and charge transport, and limits the PCEs of OSCs. In this work, ST-OSCs based on a sequentially processed heterojunction (SHJ) structure were fabricated. Through sequentially spin-coating donor PM6 as the bottom layer and acceptor Y6 as the top layer, a better vertical phase distribution is formed in the SHJ structure compared with that in the traditional bulk heterojunction (BHJ) structure. At a PM6:Y6 ratio of 1:2, the ST-OSCs based on the SHJ structure show a PCE of 12.6% at an AVT of 25.4%, while the BHJ ST-OSCs show a PCE of 11.8% at an AVT of 22.9%.

Received 24th October 2022,
Accepted 14th December 2022

DOI: 10.1039/d2tc04507a

rsc.li/materials-c

10th Anniversary Statement

Since the *Journal of Materials Chemistry C* was founded in 2013, I have been an associate editor of this journal for nearly 10 years. I am very happy that I have had such a precious opportunity to serve my beloved journal. I witnessed the launching, growing and flourishing of this journal. I am so proud of this journal since it is well recognized as one of the renowned journals in chemistry and materials science, especially as one of the most important journals in the field of electronics and photonics. I have co-authored 16 papers in this journal, and would like to further contribute and support this journal. Congratulations and happy birthday to the 10th anniversary of the *Journal of Materials Chemistry C*.

Introduction

Organic solar cells (OSCs) have attracted much interest in academia and industry owing to their merits, *e.g.* light weight, excellent flexibility, facile printing fabrication, and short energy payback time.¹ Thanks to the creation of fused-ring electron acceptors^{2,3} represented by the star molecules ITIC⁴ and Y6,⁵

the champion power conversion efficiencies (PCEs) of OSCs have surpassed 19% for single-junction devices and 20% for tandem-junction devices.^{6–8} Considering that about half of the solar emission is located at the infrared region, semitransparent OSCs (ST-OSCs), in which visible light can pass through and infrared light is used for photon–electron conversion, have become a good candidate in transparent facilities, *e.g.* building-integrated photovoltaics and power-generating windows.^{9–14}

The average visible transmittance (AVT) and PCE values are the key parameters to evaluate the ST-OSC performance. In order to achieve simultaneous enhancement of the AVT and PCE, considerable research has focused on optimizing the interfacial layers and photoactive layers,^{15–18} adopting transparent electrodes (*e.g.* ultrathin metals, conducting polymers, Ag nanowires and graphene)^{19–25} and designing novel optical structures.^{26–29} For optimizing the photoactive layers, reducing the donor content can decrease the light absorption in the visible region and increase the AVT values of ST-OSCs.^{30–33}

^a School of Materials Science and Engineering, Peking University, Beijing 100871, China. E-mail: xwzhan@pku.edu.cn

^b Key Laboratory of Eco-functional Polymer Materials of Ministry of Education, College of Chemistry and Chemical Engineering, Northwest Normal University, Lanzhou 730070, China

^c State Key Laboratory for Mechanical Behavior of Materials, Xi'an Jiaotong University, Xi'an 710049, China

^d Frontier Institute of Science and Technology, Xi'an Jiaotong University, Xi'an 710049, China

^e Jiangzhong Cancer Research Center, Jiangxi University of Chinese Medicine, Nanchang 330004, China

† Electronic supplementary information (ESI) available. See DOI: <https://doi.org/10.1039/d2tc04507a>

However, decreasing the donor content in D:A blends reduces the D/A interfacial areas, which is unfavorable for exciton dissociation and charge transport, and limits the PCE of OSCs. Therefore, developing an efficient strategy to improve charge transport in diluted donor-based ST-OSCs is necessary.

A sequentially processed heterojunction (SHJ) structure, which is fabricated through a two-step sequential solution process, exhibits similar or even better performance compared with bulk heterojunction (BHJ) structures for OSCs.^{34–37} On the one hand, the sequential solution process of donor and acceptor materials ensures sufficient D/A interfaces for exciton dissociation. On the other hand, slightly increased donor or acceptor contents at the interface of the photoactive layer/charge-transporting layer are beneficial for charge transport and charge collection owing to reduced charge recombination. Thus, fabricating ST-OSCs with SHJ structures helps to enhance charge transport, especially for ST-OSCs with low donor contents.

In this work, we fabricated ST-OSCs with a SHJ structure and diluted donor content to simultaneously improve the PCE and AVT. The wide-bandgap polymer PM6 was chosen as the donor³⁸ and the narrow-bandgap small molecule Y6 was chosen as the acceptor (Fig. 1a).⁵ Firstly, we decreased the donor content in the D:A blend (BHJ structure) in order to reduce light absorption in visible region and increase the device AVT. Then, we fabricated SHJ devices using low donor contents to enhance charge transport and collection. As a result, SHJ ST-OSCs based on a D:A ratio of 1:2 exhibited a PCE of 12.5% and an AVT of

25.4%. In contrast, BHJ ST-OSCs based on a D:A ratio of 1:2 showed a PCE of 11.8% and an AVT of 22.9%; BHJ ST-OSCs based on a D:A ratio of 1:1 showed a PCE of 11.6% and an AVT of 21.5%.

Results and discussion

Photovoltaic properties

The PM6 film has a strong absorption at *ca.* 450–650 nm, while the Y6 film shows a broad absorption ranging from 600 nm to 900 nm, which is complementary with that of PM6 (Fig. 1b). Compared with the 1:1 BHJ blend film, the maximum absorption peak of the 1:2 BHJ blend film red-shifts from 624 nm to 809 nm (Fig. 1c). Decreasing donor content and increasing acceptor content are beneficial for reducing light absorption in the visible region and harvesting more photons in the near-infrared region. The 1:2 SHJ blend film exhibits a similar light absorption compared with the 1:2 BHJ blend film, with only slight reduction at 300–600 nm.

For the BHJ device, the donor:acceptor mixture was dissolved in advance and spin-coated in one step. For the SHJ device, the donor was deposited first, followed by spin coating of the acceptor solution, as shown in Fig. S1a (ESI[†]). To explore the photovoltaic performance of different PM6:Y6 blends, we firstly fabricated opaque devices with the structure of indium tin oxide (ITO) glass/PEDOT:PSS/active layer/PNDIT-F3N/Ag (Fig. S1b, ESI[†]). The thickness of the active layer was *ca.*

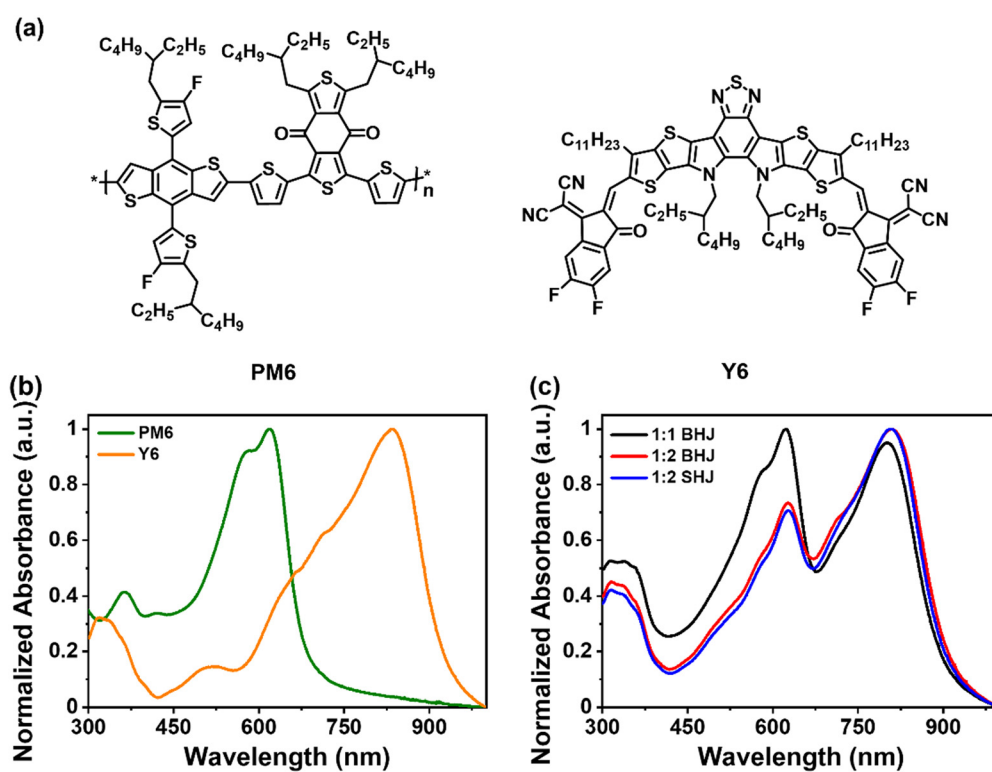


Fig. 1 (a) Chemical structures of PM6 and Y6. (b) Normalized absorption spectra of PM6 and Y6 films. (c) Normalized absorption spectra of 1:1 BHJ, 1:2 BHJ and 1:2 SHJ films.

Table 1 Performance of the 1:1 BHJ, 1:2 BHJ and 1:2 SHJ devices^a

| Type | Device structure | V_{OC} (V) | J_{SC} (mA cm $^{-2}$) | FF (%) | PCE (%) | Calc. J_{SC} (mA cm $^{-2}$) | AVT (%) |
|--------|------------------|-----------------------|---------------------------|-------------------|-------------------|---------------------------------|---------|
| Opaque | 1:1 BHJ | 0.868 (0.858 ± 0.007) | 25.6 (25.4 ± 0.4) | 67.2 (66.9 ± 1.2) | 14.9 (14.5 ± 0.4) | 24.7 | — |
| | 1:2 BHJ | 0.844 (0.842 ± 0.002) | 26.2 (25.9 ± 0.6) | 67.9 (66.7 ± 1.6) | 15.0 (14.5 ± 0.3) | 25.0 | — |
| | 1:2 SHJ | 0.842 (0.840 ± 0.002) | 26.9 (26.4 ± 0.4) | 71.1 (69.8 ± 0.9) | 16.1 (15.5 ± 0.4) | 25.6 | — |
| ST | 1:1 BHJ | 0.851 (0.852 ± 0.003) | 20.6 (20.1 ± 0.5) | 66.2 (65.4 ± 0.9) | 11.6 (11.2 ± 0.3) | 20.1 | 21.5 |
| | 1:2 BHJ | 0.831 (0.831 ± 0.003) | 21.1 (20.9 ± 0.2) | 67.5 (67.0 ± 0.5) | 11.8 (11.6 ± 0.1) | 20.6 | 22.9 |
| | 1:2 SHJ | 0.831 (0.831 ± 0.006) | 21.4 (20.8 ± 0.6) | 70.6 (69.0 ± 1.1) | 12.5 (11.9 ± 0.4) | 20.5 | 25.4 |

^a Average values (in parentheses) are obtained from 15 devices.

100 nm and the D:A weight ratios varied from 1:1 to 1:2. The 1:1 BHJ device exhibited a PCE of 14.9% with an open-circuit voltage (V_{OC}) of 0.868 V, a short-circuit current density (J_{SC}) of 25.6 mA cm $^{-2}$, and a fill factor (FF) of 67.2%. The 1:2 BHJ device exhibited a relatively lower V_{OC} of 0.844 V, a higher J_{SC} of 26.2 mA cm $^{-2}$, a similar FF of 67.9% and a comparable PCE of 15.0%. Compared with the 1:2 BHJ device, the 1:2 SHJ device delivered a high PCE of 16.1% with a similar V_{OC} of 0.842 V, a J_{SC} of 26.9 mA cm $^{-2}$ and a significantly improved FF of 71.1% (Table 1). The current density–voltage (J – V) curves of the above devices under AM 1.5G illumination (100 mW cm $^{-2}$) and corresponding external quantum efficiency (EQE) spectra are shown in Fig. 2a and b. The integrated J_{SC} values of the above three devices are 24.7, 25.0 and 25.6 mA cm $^{-2}$ (Table 1), which are consistent with the J – V results (mismatch less than 5%).

Then, we fabricated semitransparent devices with the structure of ITO glass/PEDOT:PSS/active layer/PNDIT-F3N/Au/Ag

(Fig. S1c, ESI \dagger). During ultrathin Ag electrode evaporation, Ag atoms tend to form discontinuous silver islands, which decreases the conductivity and transmittance of the Ag electrode. The ultrathin Au layer (*ca.* 1 nm) was vacuum-deposited onto the cathode interfacial layer, which can improve the uniformity and continuity of the ultrathin Ag electrode. Through adjusting the thickness of the Ag electrode, a series of ST-OSCs based on 1:1 BHJ, 1:2 BHJ and 1:2 SHJ have been fabricated (Table S1, ESI \dagger). The ST-OSCs based on the 1:1 BHJ exhibit PCEs varying from 11.6% to 12.9%, with AVT values changing from 21.5% to 11.7%. The ST-OSCs based on the 1:2 BHJ exhibit PCEs varying from 11.8% to 12.6%, with AVT values changing from 22.9% to 12.2%. The ST-OSCs based on the 1:2 SHJ exhibit PCEs varying from 12.5% to 14.0%, with AVT values changing from 25.4% to 12.6%. The optimized ST-OSCs (Au layer: 1 nm; Ag layer: 10 nm) based on the 1:1 BHJ and 1:2 BHJ exhibited similar FFs of 66.2% and 67.5%, and comparable

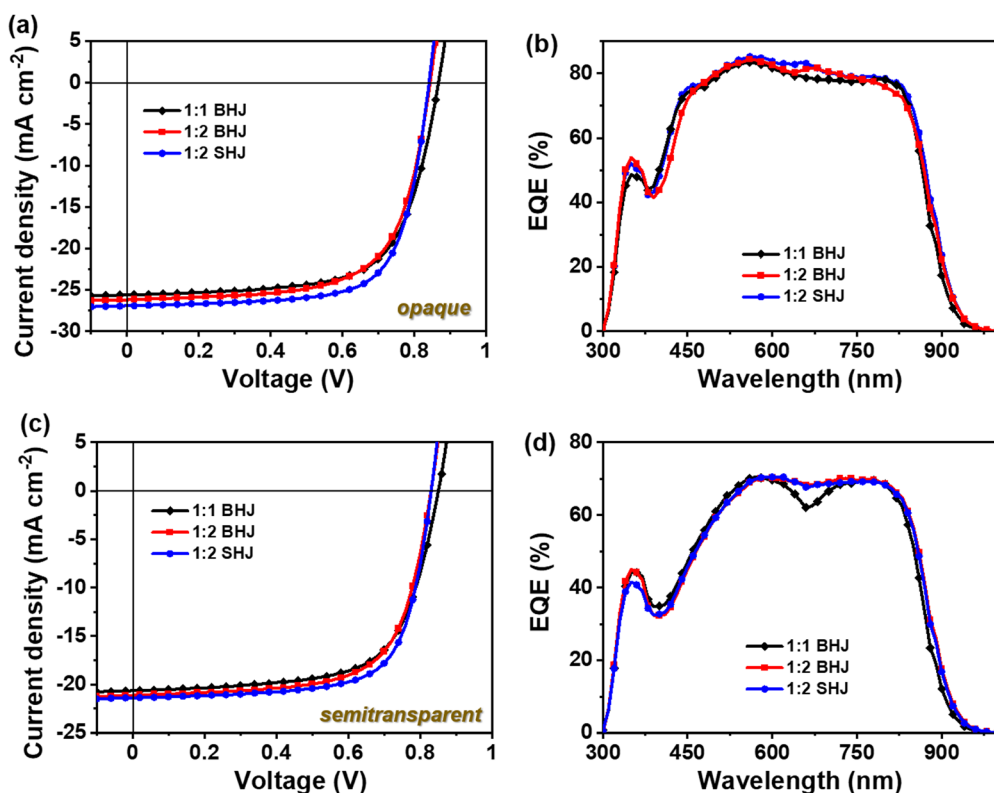


Fig. 2 (a) J – V curves and (b) EQE spectra of 1:1 BHJ, 1:2 BHJ and 1:2 SHJ opaque devices. (c) J – V curves and (d) EQE spectra of 1:1 BHJ, 1:2 BHJ and 1:2 SHJ semitransparent devices.

PCEs of 11.6% and 11.8%, respectively. Compared with the BHJ devices, the 1:2 SHJ device delivered a higher PCE of 12.5% with a significantly improved FF of 70.6% (Table 1 and Fig. 2c, d).

Optical characterization

Firstly, we investigated the optical properties of the 1:1 BHJ, 1:2 BHJ and 1:2 SHJ blend films, in which light-absorbing selectivity is one of the most important values. The light-absorbing selectivity is related to the light absorption and transmission ability in the visible region. The visible region is defined from 370 to 740 nm. By integrating the solar spectrum, the invisible photon energy power is calculated to be 48.02 mW cm^{-2} and the visible photon energy power is calculated to be 51.98 mW cm^{-2} . The light-absorbing selectivity is defined as the product of absorbed energy ratio in the invisible region and transmitted energy ratio in the visible region as follows:

$$S = \frac{\int_{280}^{370} A(\lambda) \Phi(\lambda) d\lambda + \int_{740}^{1240} A(\lambda) \Phi(\lambda) d\lambda}{48.02} \times \frac{\int_{370}^{740} T(\lambda) \Phi(\lambda) d\lambda}{51.98} \quad (1)$$

where S is the light-absorbing selectivity of the active layers, $A(\lambda)$ is the absorbance of the blend films, $T(\lambda)$ is the transmittance of the blend films and $\Phi(\lambda)$ is the solar spectrum.²⁷ The absorption and transmission spectra of the 1:1 BHJ, 1:2 BHJ and 1:2 SHJ films are shown in Fig. 1c and 3a, respectively. The light-absorbing selectivity of the 1:2 SHJ film is 0.1414, higher than that of the 1:1 BHJ film (0.1302) and the 1:2 BHJ film (0.1386), which indicates that the 1:2 SHJ film is more suitable for fabricating ST-OSCs.

Then, we investigated the optical properties of the ST-OSCs. Fig. 3b displays the transmittance spectra of devices based on

1:1 BHJ, 1:2 BHJ and 1:2 SHJ structures. In order to describe the visibility of ST-OSCs, we calculated the average photopic transmission (APT) by the integration of the transmission spectrum and AM 1.5G photo flux weighted against the photo response of the human eye as follows

$$\text{APT} = \frac{\int T(\lambda) V(\lambda) \Phi(\lambda) d\lambda}{\int V(\lambda) \Phi(\lambda) d\lambda} \quad (2)$$

where $T(\lambda)$ is the transmittance of the ST-OSCs, $\Phi(\lambda)$ is the solar spectrum, $V(\lambda)$ is the photopic response and λ ranges from 300 nm to 900 nm.³⁹ The APT values of the optimized 1:1 BHJ, 1:2 BHJ and 1:2 SHJ ST-OSCs were 17.6%, 20.2% and 22.9%, respectively. Apart from PCE, AVT and APT, light utilization efficiency (LUE) is another figure of merit to evaluate ST-OSCs (LUE = PCE \times APT). The LUEs were calculated to be 2.04%, 2.38% and 2.86% for the 1:1 BHJ, 1:2 BHJ and 1:2 SHJ ST-OSCs, respectively. Among the three different kinds of ST-OSCs, the 1:2 SHJ device exhibited the best optical performance.

The Commission Internationale de L'Eclairage (CIE) 1931 chromaticity diagram describes the transparency color perceptions of the ST-OSCs (Fig. 3c). The colour coordinates of the 1:1 BHJ, 1:2 BHJ and 1:2 SHJ devices were (0.2448, 0.2594), (0.2471, 0.2669) and (0.2534, 0.2733). The corresponding correlated color temperatures (CCT) were 19 439, 17 133 and 14 905 K (Table S2, ESI†), respectively. These values indicate that transmitted light of the 1:2 SHJ devices has a more neutral color sensation. Thus, the devices with SHJ structure show excellent visible light transparency.

Device physics and film morphology

In order to understand the reason for the FF enhancement in SHJ-based ST-OSCs, we investigated the device physics and

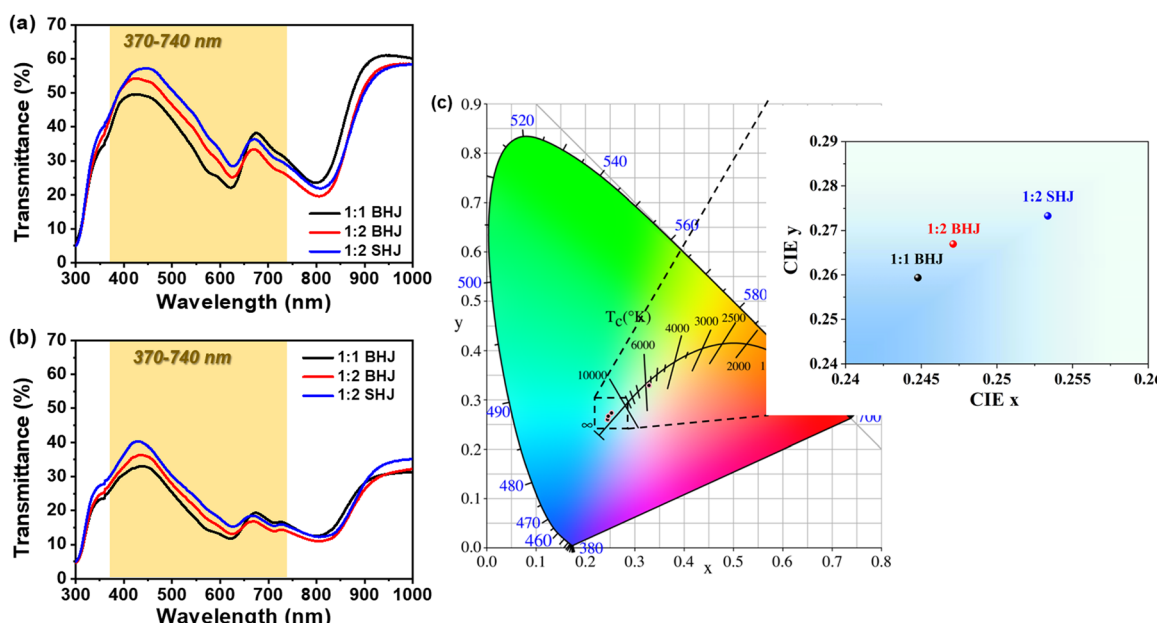


Fig. 3 Transmittance spectra of (a) blend films and (b) the corresponding ST-OSCs based on 1:1 BHJ, 1:2 BHJ and 1:2 SHJ. (c) Colour coordinates of the ST-OSCs on a CIE chromaticity diagram.

active layer morphology. The exciton dissociation behavior in the devices was studied through the photocurrent density (J_{ph}) vs. effective voltage (V_{eff}) relationship (Fig. S2a, ESI[†]). The charge-transfer state dissociation probability is proportional to the ratio of J_{SC} and saturated J_{ph} (J_{sat}). The $J_{\text{SC}}/J_{\text{sat}}$ values for the optimized 1:1 BHJ, 1:2 BHJ and 1:2 SHJ devices are 96.7%, 97.2% and 97.2%, respectively, suggesting effective exciton dissociation existing in the above three devices. We further investigated the charge recombination of the 1:1 BHJ, 1:2 BHJ and 1:2 SHJ devices through J_{SC} vs. light intensity (P_{light}) relationships. According to $J_{\text{SC}} \propto P_{\text{light}}^{\alpha}$,⁴⁰ the α values are all 0.94 for the 1:1 BHJ, 1:2 BHJ and 1:2 SHJ devices, indicating weak bimolecular recombination in the above three devices (Fig. S2b, ESI[†]).

We employed the space charge limited current (SCLC) method to measure the charge mobilities of the 1:1 BHJ, 1:2 BHJ and 1:2 SHJ blend films (Fig. S2c, d and Table S3, ESI[†]).⁴¹ The μ_{h} values of the 1:1 BHJ, 1:2 BHJ and 1:2 SHJ blend films are $6.4 \times 10^{-4} \text{ cm}^2 \text{ V}^{-1} \text{ s}^{-1}$, $5.6 \times 10^{-4} \text{ cm}^2 \text{ V}^{-1} \text{ s}^{-1}$, and $6.3 \times 10^{-4} \text{ cm}^2 \text{ V}^{-1} \text{ s}^{-1}$, respectively. The electron mobilities (μ_{e}) of the above three blends are $5.4 \times 10^{-5} \text{ cm}^2 \text{ V}^{-1} \text{ s}^{-1}$, $4.4 \times 10^{-4} \text{ cm}^2 \text{ V}^{-1} \text{ s}^{-1}$, and $7.9 \times 10^{-4} \text{ cm}^2 \text{ V}^{-1} \text{ s}^{-1}$, respectively. Compared with BHJ blend films, the optimized 1:2 SHJ film exhibits higher and more balanced charge mobilities, which can reduce charge recombination and improve the FF.

Atomic force microscopy (AFM) was used to investigate the surface morphology of the 1:1 BHJ, 1:2 BHJ and 1:2 SHJ blend films (Fig. S3, ESI[†]). The root-mean-square roughness (R_{q}) values of the 1:1 BHJ, 1:2 BHJ and 1:2 SHJ blend films are 0.99 nm, 1.04 nm, and 1.10 nm, respectively, indicating smooth

surface morphology of the above three blend films. Transmission electron microscopy (TEM) was adopted to investigate the bulky morphology of the 1:1 BHJ, 1:2 BHJ and 1:2 SHJ blend films (Fig. S4, ESI[†]). The TEM images of the above three blend films are similar.

Grazing incidence wide-angle X-ray scattering (GIWAXS) characterizations were performed to evaluate the molecular packing and orientation of the pure and blend films.^{42,43} The two-dimensional GIWAXS (2D GIWAXS) patterns and corresponding 1D line-cuts along the in-plane and out-of-plane directions of the 1:1 BHJ, 1:2 BHJ and 1:2 SHJ blend films are shown in Fig. 4. All BHJ and SHJ blend films exhibit face-on preferred orientation with strong (010) peaks in the out-of-plane direction. For the 1:1 BHJ blend film, the π - π stacking peak of Y6 locates at $q_z = 1.72 \text{ \AA}^{-1}$ (d -spacing of 3.65 \AA), and the coherence length (CL) is 2.37 nm; the lamellar stacking peak of PM6 locates at $q_r = 0.29 \text{ \AA}^{-1}$ (d -spacing of 21.66 \AA), and the corresponding CL value is 5.75 nm. For the 1:2 BHJ blend film, the Y6 π - π stacking peak locates at $q_z = 1.73 \text{ \AA}^{-1}$ (d -spacing of 3.63 \AA), and CL is almost the same (2.38 nm); as for the PM6 lamellar stacking peak, it locates at $q_r = 0.29 \text{ \AA}^{-1}$ (d -spacing of 21.66 \AA), and the corresponding CL value is 5.63 nm. Compared with the BHJ blend films, the 1:2 SHJ blend film exhibits stronger molecular ordering. The π - π stacking peak of Y6 locates at $q_z = 1.74 \text{ \AA}^{-1}$ (d -spacing of 3.61 \AA), and the corresponding CL value increases to 2.68 nm. The lamellar stacking peak of PM6 also locates at $q_r = 0.29 \text{ \AA}^{-1}$ (d -spacing of 21.66 \AA), and the corresponding CL value increases to 5.81 nm. In the 1:2 SHJ blend films, the PM6 and Y6 molecules exhibit a closer π - π stacking, leading to enhanced charge transport and FF.

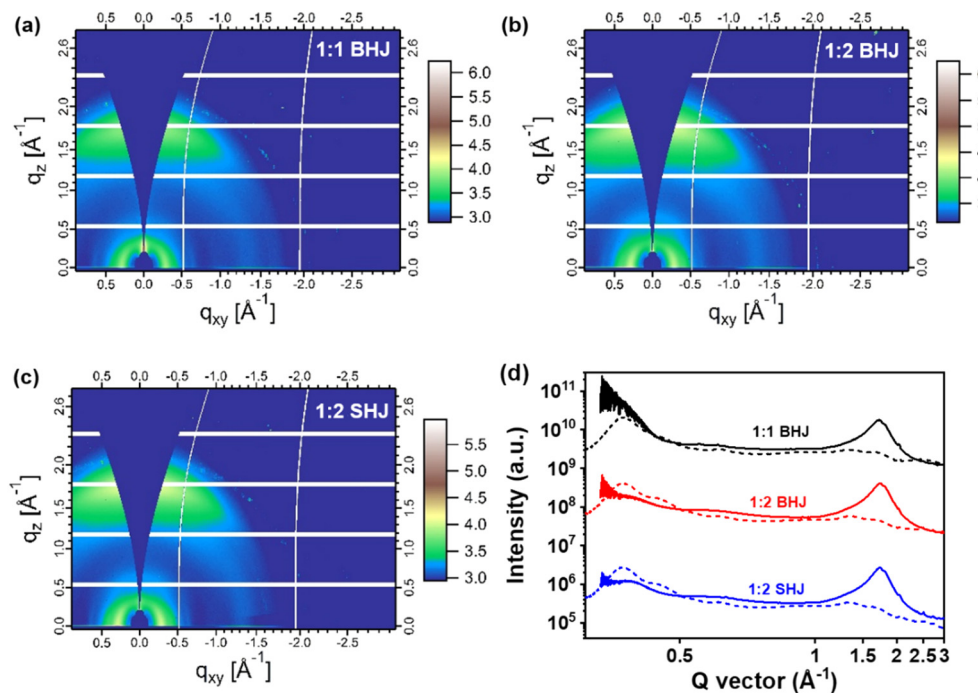


Fig. 4 2D GIWAXS patterns of (a) 1:1 BHJ, (b) 1:2 BHJ and (c) 1:2 SHJ blend films. (d) Corresponding GIWAXS 1D line-cuts along the out-of-plane (solid lines) and in-plane (dashed lines) directions.

Angle-dependent GIWAXS measurements were adopted to investigate the crystallinity change along the vertical direction.^{44–46} With larger incident angle, the X-ray beam penetrates the whole film depth, displaying an average structure of the entire film. Fig. S5 (ESI†) shows the GIWAXS 1D line-cuts of the 1:1 BHJ, 1:2 BHJ and 1:2 SHJ blend films with different incident angles (0.11°–0.15°). According to the in-plane (100) peaks ($q_{\text{r}} = 0.29 \text{ \AA}^{-1}$) and out-of-plane (010) peaks ($q_z = 1.72 \text{ \AA}^{-1}$), the lamellar stacking of the PM6 and the π – π stacking of the Y6 increase gradually with increasing incident angles. Compared to the 1:1 BHJ blend, greater enhancement of PM6 lamellar stacking can be observed for the 1:2 BHJ and 1:2 SHJ blend with increased incident angle, indicating

bottom-enriched vertical distribution of PM6 with lower D/A ratio. The backbone stacking peaks of Y6 (located at $\sim 0.4 \text{ \AA}^{-1}$) are more apparent for the 1:2 BHJ and 1:2 SHJ blend, suggesting larger phase separation than the 1:1 BHJ blend. Compared with the 1:2 BHJ blend film, the changes of PM6 lamellar stacking and Y6 π – π stacking in the 1:2 SHJ blend film are more intensive with the increased angles, indicating that the 1:2 SHJ blend film has a more pronounced vertical phase separation. Film-depth-dependent light absorption spectroscopy was used to measure the vertical distribution of donor/acceptor.^{47–49} The donor/acceptor vertical segregation is different in BHJ and SHJ films as a result of different phase evolutions during film deposition. In the 1:1 BHJ blend film, the

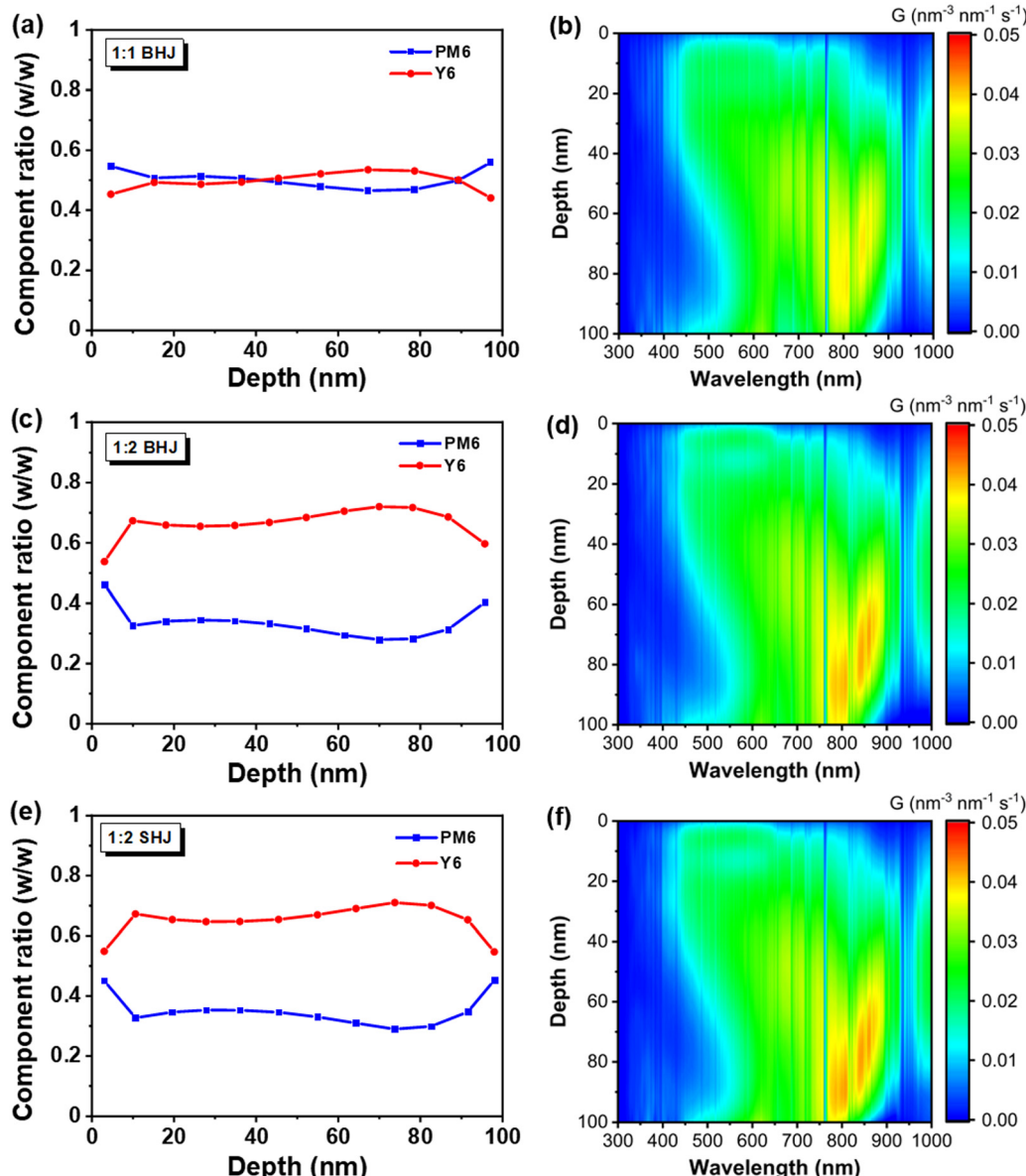


Fig. 5 Donor/acceptor composition distribution as a function of film depth for (a) 1:1 BHJ; (c) 1:2 BHJ and (e) 1:2 SHJ blend films. Exciton generation contours (unit, $10^{16} \text{ mm}^{-3} \text{ nm}^{-1} \text{ s}^{-1}$ at its position and wavelength) are calculated from the film-depth-dependent light absorption spectra (b, d and f) in combination with optical interference. The vertical noise-like lines in the contour are originally from the solar spectral profile of AM 1.5 G. The film depths 0 nm and 100 nm represent active layer/PNDIT-F3N and PEDOT:PSS/active layer interfaces, respectively.

PM6 and Y6 materials exhibit no obvious phase separation in the vertical direction. The content of PM6 is slightly lower than that of Y6 in the lower half of the active layer (50–90 nm), and is slightly higher in the upper half (0–50 nm), which is not beneficial for charge transport and collection, leading to relatively lower J_{SC} and FF. In the 1:2 BHJ blend film, the content of Y6 is >50% in the entire device. However, relatively high content of Y6 near the anode is not good for collecting holes, which still limits the FF of the devices. In contrast, in the 1:2 SHJ blend film, the vertical phase distribution is optimized. In the upper half of the active layer, especially at the active layer/PNDIT-F3N interface, the Y6 content is increased. In the lower half of the active layer, the PM6 content is increased, and can even reach 50% at the interface (Fig. 5a, c and e). The improved vertical phase distribution is beneficial for reducing charge recombination and improving charge transport, leading to higher J_{SC} and FF. Then, the exciton generation contours were calculated *via* a modified transfer-matrix method (Fig. 5b, d and f),⁵⁰ with the film-depth-dependent optical variations (Fig. S6, ESI†) as input. The maximum exciton generation rates (G_{max}) of the 1:1 BHJ, 1:2 BHJ and 1:2 SHJ blend films were calculated to be $15.06 \text{ nm}^{-3} \text{ s}^{-1}$, $15.03 \text{ nm}^{-3} \text{ s}^{-1}$ and $15.14 \text{ nm}^{-3} \text{ s}^{-1}$, respectively (Fig. S7, ESI†), and the higher G_{max} value accompanies more exciton generation, which is beneficial for J_{SC} improvement.

Conclusions

In summary, we have fabricated high-performance ST-OSCs based on wide-bandgap polymer donor PM6 and narrow-bandgap acceptor Y6, using diluted donor contents combined with a sequential solution process. Firstly, we decreased the ratio of PM6 in the PM6:Y6 BHJ blends to weaken the visible light absorption and to enhance device transparency in the visible region. Then, using low donor contents, we adopted a layer-by-layer solution process to fabricate SHJ ST-OSCs. Compared with BHJ devices, SHJ devices exhibited more proper donor/acceptor vertical separation, and higher and more balanced charge mobility, which is beneficial for increasing the FF of devices. The 1:2 SHJ ST-OSCs showed higher PCE, higher AVT and higher LUE than the BHJ counterpart. This work presented a useful method to achieve ST-OSCs with high efficiency and high transparency.

Conflicts of interest

The authors declare no conflict of interest.

Acknowledgements

X. Z. thanks the NSFC (No. U21A20101). W. M. thanks the NSFC (21704082, 21875182), Key Scientific and Technological Innovation Team Project of Shaanxi Province (2020TD-002), and 111 Project 2.0 (BP2018008). GIWAXS data were acquired at beamlines 7.3.3 at the Advanced Light Source, which is supported by

the Director, Office of Science, Office of Basic Energy Sciences, of the U.S. Department of Energy under Contract No. DE-AC02-05CH11231. The authors thank Dr Eric Schaible and Dr Chen-hui Zhu at beamline 7.3.3 for assistance with data acquisition.

Notes and references

- 1 L. Lu, T. Zheng, Q. Wu, A. M. Schneider, D. Zhao and L. Yu, *Chem. Rev.*, 2015, **115**, 12666–12731.
- 2 C. Yan, S. Barlow, Z. Wang, H. Yan, A. K. Y. Jen, S. R. Marder and X. Zhan, *Nat. Rev. Mater.*, 2018, **3**, 18003.
- 3 J. Wang, P. Xue, Y. Jiang, Y. Huo and X. Zhan, *Nat. Rev. Chem.*, 2022, **6**, 614–634.
- 4 Y. Lin, J. Wang, Z.-G. Zhang, H. Bai, Y. Li, D. Zhu and X. Zhan, *Adv. Mater.*, 2015, **27**, 1170–1174.
- 5 J. Yuan, Y. Zhang, L. Zhou, G. Zhang, H.-L. Yip, T.-K. Lau, X. Lu, C. Zhu, H. Peng, P. A. Johnson, M. Leclerc, Y. Cao, J. Ulanski, Y. Li and Y. Zou, *Joule*, 2019, **3**, 1140–1151.
- 6 C. He, Y. Pan, Y. Ouyang, Q. Shen, Y. Gao, K. Yan, J. Fang, Y. Chen, C. Ma, J. Min, C. Zhang, L. Zuo and H. Chen, *Energy Environ. Sci.*, 2022, **15**, 2537–2544.
- 7 R. Sun, Y. Wu, X. Yang, Y. Gao, Z. Chen, K. Li, J. Qiao, T. Wang, J. Guo, C. Liu, X. Hao, H. Zhu and J. Min, *Adv. Mater.*, 2022, **34**, 2110147.
- 8 Z. Zheng, J. Wang, P. Bi, J. Ren, Y. Wang, Y. Yang, X. Liu, S. Zhang and J. Hou, *Joule*, 2022, **6**, 171–184.
- 9 Y. Li, X. Guo, Z. Peng, B. Qu, H. Yan, H. Ade, M. Zhang and S. R. Forrest, *Proc. Natl. Acad. Sci. U. S. A.*, 2020, **117**, 21147–21154.
- 10 C. Sun, R. Xia, H. Shi, H. Yao, X. Liu, J. Hou, F. Huang, H.-L. Yip and Y. Cao, *Joule*, 2018, **2**, 1816–1826.
- 11 J. Wang, J. Zhang, Y. Xiao, T. Xiao, R. Zhu, C. Yan, Y. Fu, G. Lu, X. Lu, S. R. Marder and X. Zhan, *J. Am. Chem. Soc.*, 2018, **140**, 9140–9147.
- 12 S. Dai and X. Zhan, *Adv. Energy Mater.*, 2018, **8**, 1800002.
- 13 W. Wang, C. Yan, T.-K. Lau, J. Wang, K. Liu, Y. Fan, X. Lu and X. Zhan, *Adv. Mater.*, 2017, **29**, 1701308.
- 14 T. Li, S. Dai, Z. Ke, L. Yang, J. Wang, C. Yan, W. Ma and X. Zhan, *Adv. Mater.*, 2018, **30**, 1705969.
- 15 P. Yin, Z. Yin, Y. Ma and Q. Zheng, *Energy Environ. Sci.*, 2020, **13**, 5177–5185.
- 16 X. Huang, L. Zhang, Y. Cheng, J. Oh, C. Li, B. Huang, L. Zhao, J. Deng, Y. Zhang, Z. Liu, F. Wu, X. Hu, C. Yang, L. Chen and Y. Chen, *Adv. Funct. Mater.*, 2021, **32**, 2108634.
- 17 P. Cheng, H.-C. Wang, Y. Zhu, R. Zheng, T. Li, C.-H. Chen, T. Huang, Y. Zhao, R. Wang, D. Meng, Y. Li, C. Zhu, K.-H. Wei, X. Zhan and Y. Yang, *Adv. Mater.*, 2020, **32**, 2003891.
- 18 J. Zhang, G. Xu, F. Tao, G. Zeng, M. Zhang, Y. Yang, Y. Li and Y. Li, *Adv. Mater.*, 2019, **31**, 1807159.
- 19 Y. Wang, B. Jia, F. Qin, Y. Wu, W. Meng, S. Dai, Y. Zhou and X. Zhan, *Polymer*, 2016, **107**, 108–112.
- 20 H. Park, J.-H. Lee, S. Lee, S. Y. Jeong, J. W. Choi, C.-L. Lee, J.-H. Kim and K. Lee, *ACS Appl. Mater. Interfaces*, 2020, **12**, 2276–2284.

21 Z. Liu, P. You, S. Liu and F. Yan, *ACS Nano*, 2015, **9**, 12026–12034.

22 L. Qin, J. Jiang, Q. Tao, C. Wang, I. Persson, M. Fahlman, P. O. Å. Persson, L. Hou, J. Rosen and F. Zhang, *J. Mater. Chem. A*, 2020, **8**, 5467–5475.

23 M. P. Ramuz, M. Vosgueritchian, P. Wei, C. Wang, Y. Gao, Y. Wu, Y. Chen and Z. Bao, *ACS Nano*, 2012, **6**, 10384–10395.

24 J. Min, C. Bronnbauer, Z.-G. Zhang, C. Cui, Y. N. Luponosov, I. Ata, P. Schweizer, T. Przybilla, F. Guo, T. Ameri, K. Forberich, E. Spiecker, P. Bäuerle, S. A. Ponomarenko, Y. Li and C. J. Brabec, *Adv. Funct. Mater.*, 2016, **26**, 4543–4550.

25 G. Ji, Y. Wang, Q. Luo, K. Han, M. Xie, L. Zhang, N. Wu, J. Lin, S. Xiao, Y.-Q. Li, L.-Q. Luo and C.-Q. Ma, *ACS Appl. Mater. Interfaces*, 2018, **10**, 943–954.

26 Q. Liu, L. G. Gerling, F. Bernal-Texca, J. Toudert, T. Li, X. Zhan and J. Martorell, *Adv. Energy Mater.*, 2020, **10**, 1904196.

27 Y. Li, C. He, L. Zuo, F. Zhao, L. Zhan, X. Li, R. Xia, H.-L. Yip, C.-Z. Li, X. Liu and H. Chen, *Adv. Energy Mater.*, 2021, **11**, 2003408.

28 R. Betancur, P. Romero-Gomez, A. Martinez-Otero, X. Elias, M. Maymó and J. Martorell, *Nat. Photonics*, 2013, **7**, 995–1000.

29 Y. Li, C. Ji, Y. Qu, X. Huang, S. Hou, C.-Z. Li, L.-S. Liao, L. J. Guo and S. R. Forrest, *Adv. Mater.*, 2019, **31**, 1903173.

30 N. Schopp, G. Akhtanova, P. Panoy, A. Arbuz, S. Chae, A. Yi, H. J. Kim, V. Promarak, T.-Q. Nguyen and V. V. Brus, *Adv. Mater.*, 2022, **34**, 2203796.

31 Y. Tang, H. Zheng, X. Zhou, Z. Tang, W. Ma and H. Yan, *Small Methods*, 2022, **6**, 2101570.

32 Y. Xie, Y. Cai, L. Zhu, R. Xia, L. Ye, X. Feng, H.-L. Yip, F. Liu, G. Lu, S. Tan and Y. Sun, *Adv. Funct. Mater.*, 2020, **30**, 2002181.

33 Z. Hu, Z. Wang and F. Zhang, *J. Mater. Chem. A*, 2019, **7**, 7025–7032.

34 K. Jiang, J. Zhang, Z. Peng, F. Lin, S. Wu, Z. Li, Y. Chen, H. Yan, H. Ade, Z. Zhu and A. K.-Y. Jen, *Nat. Commun.*, 2021, **12**, 468.

35 L. Zhan, S. Li, X. Xia, Y. Li, X. Lu, L. Zuo, M. Shi and H. Chen, *Adv. Mater.*, 2021, **33**, 2007231.

36 H. Ning, Q. Jiang, P. Han, M. Lin, G. Zhang, J. Chen, H. Chen, S. Zeng, J. Gao, J. Liu, F. He and Q. Wu, *Energy Environ. Sci.*, 2021, **14**, 5919–5928.

37 Y. Wang and X. Zhan, *Adv. Energy Mater.*, 2016, **6**, 1600414.

38 M. Zhang, X. Guo, W. Ma, H. Ade and J. Hou, *Adv. Mater.*, 2015, **27**, 4655–4660.

39 C. Yang, D. Liu, M. Bates, M. C. Barr and R. R. Lunt, *Joule*, 2019, **3**, 1803–1809.

40 P. Schilinsky, C. Waldauf and C. J. Brabec, *Appl. Phys. Lett.*, 2002, **81**, 3885–3887.

41 G. G. Malliaras, J. R. Salem, P. J. Brock and C. Scott, *Phys. Rev. B: Condens. Matter Mater. Phys.*, 1998, **58**, 13411–13414.

42 F. Liu, Y. Gu, X. Shen, S. Ferdous, H.-W. Wang and T. P. Russell, *Prog. Polym. Sci.*, 2013, **38**, 1990–2052.

43 L. Zhang, X. Xu, B. Lin, H. Zhao, T. Li, J. Xin, Z. Bi, G. Qiu, S. Guo, K. Zhou, X. Zhan and W. Ma, *Adv. Mater.*, 2018, **30**, 1805041.

44 G. Renaud, R. Lazzari and F. Leroy, *Surf. Sci. Rep.*, 2009, **64**, 255–380.

45 J. Wang, M. J. Bedzyk and M. Caffrey, *Science*, 1992, **258**, 775–778.

46 Y. Wang, X. Wang, B. Lin, Z. Bi, X. Zhou, H. B. Naveed, K. Zhou, H. Yan, Z. Tang and W. Ma, *Adv. Energy Mater.*, 2020, **10**, 2000826.

47 L. Bu, S. Gao, W. Wang, L. Zhou, S. Feng, X. Chen, D. Yu, S. Li and G. Lu, *Adv. Electron. Mater.*, 2016, **2**, 1600359.

48 T. Xiao, J. Wang, S. Yang, Y. Zhu, D. Li, Z. Wang, S. Feng, L. Bu, X. Zhan and G. Lu, *J. Mater. Chem. A*, 2020, **8**, 401–411.

49 P. Xue, S. Dai, T.-K. Lau, J. Yu, J. Zhou, Y. Xiao, K. Meng, Z. Xie, G. Lu, X. Lu, R. P. S. Han and X. Zhan, *Sol. RRL*, 2020, **4**, 2000115.

50 Y. Huo, X.-T. Gong, T.-K. Lau, T. Xiao, C. Yan, X. Lu, G. Lu, X. Zhan and H.-L. Zhang, *Chem. Mater.*, 2018, **30**, 8661–8668.